
EigenScore: OOD Detection using Posterior Covariance in Diffusion Models

Shirin Shoushtari Yi Wang Xiao Shi
M. Salman Asif Ulugbek S. Kamilov

Washington University in St. Louis
{s.shirin, y.wang1, shi.xiao, kamilov}@wustl.edu
University of California, Riverside
sasif@ucr.edu

Abstract

Out-of-distribution (OOD) detection is critical for the safe deployment of machine learning systems in safety-sensitive domains. Diffusion models have recently emerged as powerful generative models, capable of capturing complex data distributions through iterative denoising. Building on this progress, recent work has explored their potential for OOD detection. We propose *EigenScore*, a new OOD detection method that leverages the eigenvalue spectrum of the posterior covariance induced by a diffusion model. We argue that posterior covariance provides a consistent signal of distribution shift, leading to larger trace and leading eigenvalues on OOD inputs, yielding a clear spectral signature. We further provide analysis explicitly linking posterior covariance to distribution mismatch, establishing it as a reliable signal for OOD detection. To ensure tractability, we adopt a Jacobian-free subspace iteration method to estimate the leading eigenvalues using only forward evaluations of the denoiser. Empirically, EigenScore achieves SOTA performance, with up to 5% AUROC improvement over the best baseline. Notably, it remains robust in near-OOD settings such as CIFAR-10 vs CIFAR-100, where existing diffusion-based methods often fail.

1 introduction

Most machine learning systems assume that test data matches the training distribution, but distribution shift or out-of-distribution (OOD) data can severely degrade performance in safety-critical domains such as medical imaging and autonomous driving [1]. OOD inputs may stem from sensor noise, semantic differences, or acquisition changes, leading to unreliable predictions [2]. To address this, many OOD detection methods have been proposed, ranging from supervised approaches that require labeled OOD data to unsupervised approaches that rely only on in-distribution (InD) training data [3].

Existing OOD detection methods can be broadly categorized into four families: (i) **uncertainty-based** methods, which rely on signals such as softmax confidence [4], ensemble variance [5], or Bayesian inference [6, 7] to identify anomalous inputs; (ii) **distance-based** methods [8], which compare test embeddings to in-distribution features, commonly via Mahalanobis distance [9, 10]; (iii) **density-based** methods [11], including flow- and energy-based models [12, 13], which attempt to estimate likelihoods but have been shown to assign spuriously high likelihoods to OOD data [14]; and (iv) **representation-learning** methods [15], including self-supervised and contrastive techniques [16–18], which improve robustness by explicitly shaping feature spaces (Also see reviews in [19, 20]).

Diffusion models (DMs) [21, 22] have emerged as state-of-the-art generative models, achieving high-quality samples across diverse domains. Their success has spurred both architectural advances [23–26] and applications beyond generation, such as imaging inverse problems and medical tasks [27, 28] (see also recent reviews [29–32]). Crucially, diffusion models are especially relevant for OOD detection because their iterative denoising process does not simply produce samples, but also provides access to score functions that explicitly characterize the data distribution. Early work exploited this property through likelihood- or reconstruction-based scores [3, 33, 34]. More recent studies

have explored structural aspects of the diffusion trajectory, such as score geometry and intermediate representations [3, 35–37]. These developments highlight both the promise of diffusion-based OOD methods and the need for principled approaches that move beyond heuristic scoring rules.

Building on recent work in diffusion-based OOD detection, we introduce **EigenScore**, an unsupervised, feature-based framework for identifying distribution shift. Unlike reconstruction-based methods that measure input–output similarity [3] or trajectory-based methods that analyze diffusion-path geometry [35], EigenScore leverages the covariance structure of the denoising process to capture uncertainty signals. By linking posterior covariance, estimated from the denoiser’s Jacobian, to distribution shift, EigenScore provides a theoretically grounded and interpretable signal while remaining practical at scale through a Jacobian-free eigenvalue estimation algorithm. Our analysis, supported by both theory and experiments, shows that applying an in-distribution diffusion model to OOD samples leads to inflated posterior covariance. This effect provides a stable and discriminative signal for OOD detection. Our contributions are threefold:

- We introduce **EigenScore**, an unsupervised, feature-based framework for OOD detection in diffusion models. EigenScore leverages the posterior covariance of the denoising process to characterize distribution shift.
- We provide supporting analysis establishing a direct connection between denoising uncertainty from posterior covariance and distribution mismatch, thereby explaining why EigenScore reliably separates InD from OOD samples.
- We conduct extensive experiments on standard OOD benchmarks (CIFAR-10 (C10), CIFAR-100 (C100), SVHN, CelebA, TinyImageNet), showing that EigenScore achieves average state-of-the-art performance and remains notably robust in challenging near-OOD scenarios.

2 Background

Diffusion Models. Diffusion models learn to generate samples by simulating a gradual denoising process. During training, a clean sample $\mathbf{x} \sim p(\mathbf{x})$ is perturbed by Gaussian noise across timesteps $t = 1, \dots, T$, producing noisy states \mathbf{x}_t through the forward Markov chain $p(\mathbf{x}_t|\mathbf{x}) = \mathcal{N}(\mathbf{x}, \sigma_t^2 \mathbf{I})$, which allows for direct sampling via $\mathbf{x}_t = \mathbf{x} + \mathbf{z}$, where $\mathbf{z} \sim \mathcal{N}(0, \sigma_t^2 \mathbf{I})$.

The reverse process is approximated by a denoising network $D_\theta(\mathbf{x}_t, t)$, trained to predict either the clean signal or the injected noise. A standard training objective is mean squared error (MSE):

$$\mathcal{L}_{\text{MSE}}(D_\theta) = \mathbb{E}_{\mathbf{x}, \mathbf{x}_t, t} \left[\left\| \mathbf{x} - D_\theta(\mathbf{x}_t, t) \right\|_2^2 \right]. \quad (1)$$

Once trained, the model generates new samples by iteratively denoising from Gaussian noise at $t = T$ back to $t = 0$. Importantly, Tweedie’s formula [38, 39] connects Gaussian denoising with score estimation, linking the posterior mean to the gradient of the log-density as

$$D_p(\mathbf{x}_t) = \mathbb{E}_p[\mathbf{x}|\mathbf{x}_t] = \mathbf{x}_t + \sigma_t^2 \nabla \log p(\mathbf{x}_t), \quad (2)$$

where $D_p(\mathbf{x}_t)$ denotes an MMSE estimator trained on samples from distribution p . Here, the gradient is with respect to \mathbf{x}_t , and $p(\mathbf{x}_t)$ denotes the marginal distribution noisy image

$$p(\mathbf{x}_t) = \int p(\mathbf{x}_t|\mathbf{x})p(\mathbf{x})d\mathbf{x} = \int G_{\sigma_t}(\mathbf{x}_t - \mathbf{x})p(\mathbf{x})d\mathbf{x}, \quad (3)$$

where G_{σ_t} denotes the Gaussian density function with standard deviation $\sigma_t \geq 0$ [40, 41]. This relationship implies that denoising does more than produce samples—it provides access to score functions and posterior statistics of the underlying distribution. In the context of OOD detection, this observation motivates our use of the denoiser’s covariance structure as a principled signal of distribution shift. Diffusion models admit several formulations (e.g., variance-preserving, variance-exploding, and SDE-based), but all share the key property of learning the score function $\nabla_{\mathbf{x}_t} \log p(\mathbf{x}_t)$ to guide denoising [21, 22, 42, 43].

Unsupervised OOD detection. Unsupervised OOD detection aims to determine whether a given sample \mathbf{x} originates from the same distribution as the training data, using only unlabeled InD samples $\mathbf{x}_1, \dots, \mathbf{x}_n \sim p(\mathbf{x})$. The goal is to learn a detector that assigns an OOD score to each input, where

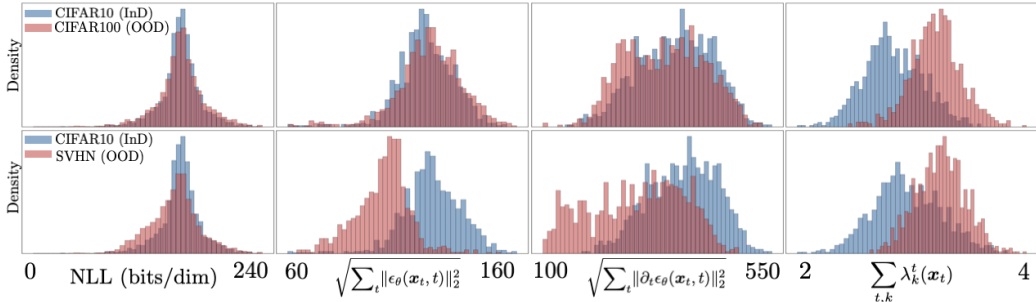


Figure 1: We compare negative log-likelihood (NLL), score norm $\sqrt{\sum_t \|\epsilon_\theta(\mathbf{x}_t, t)\|_2^2}$, score derivative norm $\sqrt{\sum_t \|\partial_t \epsilon_\theta(\mathbf{x}_t, t)\|_2^2}$, and the eigenvalue sum (ours) $\sum_{t,k} \lambda_k^t(\mathbf{x}_t)$ as OOD detection statistics. **Top row:** near OOD task for C10 (InD) vs. C100, NLL and score-based metrics fail to separate distributions, showing substantial overlap. **Bottom row:** for C10 (InD) vs. SVHN (OOD), the ordering of metrics inverts—score and derivative norms assign lower values to OOD than InD, making thresholds unreliable. In both settings, our eigenvalue-based metric achieves clear separation and consistently assigns higher scores to OOD samples.

higher scores indicate a greater likelihood that \mathbf{x} was drawn from a different distribution, such as the OOD density $q(\mathbf{x})$ [3, 35].

Likelihood-based methods. These methods use generative models including VAEs, flows, diffusion models to estimate sample likelihoods, under the assumption that OOD data should receive lower likelihoods [44–47]. However, it has been shown that generative models often assign high likelihoods to OOD inputs [5, 14, 48]. To mitigate this, refined scores have been proposed, including likelihood ratios [49], compression corrections [50], WAIC ensembles [5], and typicality tests [51]. Diffusion-based variants further extend this idea by analyzing statistics across the denoising trajectory [35, 52].

Reconstruction-based methods. Another line of work assumes that InD samples reconstruct well, whereas OOD samples do not. Early examples include autoencoders [53] and GANs [54]. More recently, diffusion models have been exploited for their strong reconstruction fidelity, leading to perceptual quality scores [3], projection regret [37], and masked inpainting methods like LMD [36].

Feature-based methods. These approaches distinguish InD from OOD by leveraging learned representations, such as Mahalanobis distance in latent space [55], unsupervised contrastive features [17, 18, 56], or encoder features from invertible models [57]. Pretrained feature extractors have also proven effective [58].

Complementing these approaches, we introduce a new perspective based on posterior covariance in diffusion models, which provides a principled feature for quantifying distribution shift.

3 Diffusion Model for Out-of-Distribution Detection

EigenScore is a novel OOD detection method that exploits covariance structure of the denoising diffusion process. Our key insight is that when a diffusion model trained on InD data is applied to OOD inputs, the variance of its denoising predictions inflates, leaving a characteristic signature in the eigenvalue spectrum of the score Jacobian.

To motivate EigenScore, we first revisit why commonly used diffusion-based OOD metrics—likelihood, score norm, and score derivatives—are unreliable (Sec. 3.1). We then show, both theoretically and empirically, that posterior covariance offers a consistent marker of distribution shift (Sec. 3.2), before formalizing EigenScore and its efficient computation (Sec. 3.3).

3.1 Why Likelihood and Score Dynamics Are Insufficient

Since diffusion models are trained via a variational lower bound (ELBO), likelihood-based scores such as negative log-likelihood (NLL) are natural candidates for OOD detection. However, likelihood does not necessarily align with semantic structure: diffusion models often emphasize low-level statistics while ignoring higher-level semantics, making NLL unreliable [50, 51]. Empirically, NLL

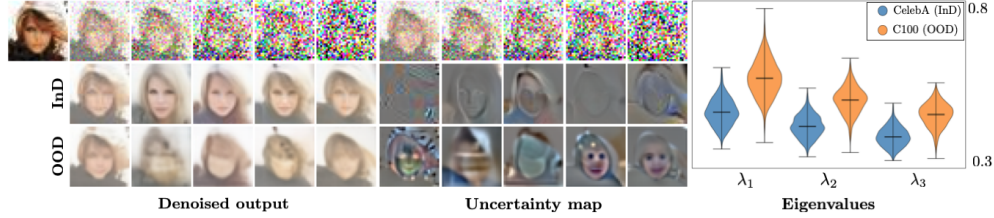


Figure 2: Denoised outputs (left), corresponding uncertainty maps (first principle component) (middle), and violin plots of the three largest eigenvalues for CelebA dataset (right). Top: clean CelebA image and its noisy variants for varying t . Middle: InD model (trained on CelebA) applied to CelebA inputs. Bottom: OOD model (trained on C100) applied to the same inputs. InD models yield sharp reconstructions and localized uncertainty with smaller leading eigenvalues, whereas OOD models produce blurrier outputs, diffuse uncertainty, and inflated eigenvalues—highlighting the eigenvalue spectrum as an indicator of distribution shift.

Algorithm 1 OOD Detection with EigenScore — Train/Validation (left) and Test (right)

Train/Validation: Select time-steps, aggregation, and compute Z-score stats

Require: Trained DM D_p , train set $\mathcal{X}_{\text{train}}$, K number of eigenvalues, I number of repetition, $L_{\text{train}} = []$

- 1: **for** $\mathbf{x} \in \mathcal{X}_{\text{train}}$ **do**
- 2: Compute $M(\mathbf{x})$ via Eq. (10)
- 3: Append $M(\mathbf{x})$ to L_{train}
- 4: **end for**
- 5: Compute μ_t, σ_t across L_{train}
- 6: Use validation set to tune T and aggregation method (mean/median/none)
- 7: **return** $(T^*, agg^*, \{\mu_t, \sigma_t\}_{t=1}^{T^*})$

Test: Compute EigenScore

Require: Trained DM D_p , test set $\mathcal{X}_{\text{test}}$, number of eigenvalues K , number of repetitions I , $(T^*, agg^*, \{\mu_t, \sigma_t\}_{t=1}^{T^*})$, $L_{\text{test}} = []$

- 1: **for** $\mathbf{x} \in \mathcal{X}_{\text{test}}$ **do**
 - 2: Compute $M(\mathbf{x})$ using T^* and agg^*
 - 3: $z_t(\mathbf{x}) = \frac{\overline{m}_t(\mathbf{x}) - \mu_t}{\sigma_t}$ for $t = 1, \dots, T^*$
 - 4: $S_\theta(\mathbf{x}) = \sum_{t=1}^{T^*} z_t(\mathbf{x})$
 - 5: Append $S_\theta(\mathbf{x})$ to L_{test}
 - 6: **end for**
 - 7: **return** L_{test} ▷ OOD scores for all test samples
-

can even assign higher likelihoods to OOD samples than to InD ones [35]. As shown in Fig. 1, NLL is not a reliable metric for separating InD from OOD samples.

Beyond likelihood, diffusion-based OOD metrics have also used the score function $\epsilon_\theta(\mathbf{x}_t, t)$ and its temporal derivative $\partial_t \epsilon_\theta(\mathbf{x}_t, t)$ as statistics [35]. Their norms provide some empirical separation, but they remain unstable. In near-OOD settings (C10 vs. C100), the distributions overlap substantially (Fig.1, top row). In some settings (C10 vs. SVHN), the ordering can invert, with OOD samples receiving lower scores than InD (Fig.1, bottom row). These limitations motivate shifting from scalarized scores toward a covariance-based perspective, where the structure of denoiser variability itself provides a more principled signal of distribution shift

3.2 Uncertainty as a Signal of Distribution Shift

We formalize why denoising uncertainty yields a principled OOD signal. Let $p(\mathbf{x})$ denote InD and $q(\mathbf{x})$ an OOD distribution. Under Gaussian corruption with variance σ_t^2 , the KL divergence admits the score-based representation [35, 59–61]

$$D_{\text{KL}}(p \parallel q) = \int_0^T \mathbb{E}_{\mathbf{x}, \mathbf{x}_t} \left[\|\nabla \log p(\mathbf{x}_t) - \nabla \log q(\mathbf{x}_t)\|_2^2 \right] \sigma_t dt. \quad (4)$$

where \mathbf{x}_t is generated by the forward diffusion applied to \mathbf{x} . Building on prior analyses of KL divergence in diffusion processes [35, 61], we restate the divergence in terms of denoising error (a derivation is given in App. A.1 for completeness).

Proposition 1. Let p_t and q_t denote the noisy marginals of InD and OOD distributions generated by the forward diffusion process (Eq. (3)). For MMSE denoisers $D_p(\mathbf{x}_t) = \mathbb{E}_p[\mathbf{x}|\mathbf{x}_t]$ and $D_q(\mathbf{x}_t) = \mathbb{E}_q[\mathbf{x}|\mathbf{x}_t]$,

$$D_{\text{KL}}(p \parallel q) = \int_0^T [MSE(D_q, t) - MSE(D_p, t)] \sigma_t^{-3} dt$$

where $MSE(D_p, t) = \mathbb{E}[\|\mathbf{x} - D_p(\mathbf{x}_t)\|_2^2]$ at noise level t .

This proposition, adapted from earlier derivations, shows that KL divergence—and thus distribution shift—can be viewed as the accumulation of *excess denoising error* incurred when contrasting the optimal MMSE denoiser under q with that under p . Thus, we have $MSE(D_p; q, t) \geq MSE(D_q; q, t)$ for each t and the denoising error of a single InD denoiser D_p is *larger in expectation* on OOD inputs, yielding a practical detection signal without access to q .

For the MMSE denoiser D_p , the mean-squared error admits a law-of-total-variance decomposition (proof in App. A.3):

$$MSE(D_p, t) = \mathbb{E}[\|\mathbf{x} - D_p(\mathbf{x}_t)\|_2^2] = \mathbb{E}_{\mathbf{x}_t}[\text{tr}(\text{Cov}_p[\mathbf{x} | \mathbf{x}_t])]. \quad (5)$$

Thus, denoising error equals the *total posterior variance*—the trace of the conditional covariance—averaged over noisy observations at noise level t . Intuitively, $\text{Cov}_p[\mathbf{x} | \mathbf{x}_t]$ quantifies the spread of plausible clean signals consistent with \mathbf{x}_t . When \mathbf{x}_t is informative (e.g., InD or low noise), this spread is small and the MSE remains low; when \mathbf{x}_t lies off-manifold, the spread inflates and the MSE increases. In this sense, denoising error corresponds directly to the model’s predictive uncertainty, providing a principled basis for OOD detection and motivating our focus on the *spectral structure* of posterior covariance in Section 3.3.

While Eq.4 relates distribution shift to differences in score norms, such metrics do not preserve ordering: depending on the dataset and noise scale, OOD samples may appear either larger or smaller than InD ones. By contrast, the MSE-based formulation in Prop.1 guarantees that OOD denoising error is systematically larger in expectation than InD error. This ensures a consistent separation with preserved ordering, whereas score-norm methods such as DiffPath [35] capture only relative differences without indicating direction.

3.3 Eigenvalue-Based Uncertainty estimation

Section 3.2 established that denoising error equals the total posterior variance and that this variance inflates under distribution shift. We now make this connection operational by expressing posterior covariance through the Jacobian of the MMSE denoiser and analyzing its eigen-spectrum. For the MMSE denoiser $D_p(\mathbf{x}_t) = \mathbb{E}[\mathbf{x}|\mathbf{x}_t]$, the posterior covariance admits the Miyasawa identity [39]:

$$\text{Cov}_p[\mathbf{x}|\mathbf{x}_t] = \sigma_t^2 (\mathbf{I} + \sigma_t^2 \nabla^2 \log p(\mathbf{x}_t)) = \sigma_t^2 \nabla D_p(\mathbf{x}_t), \quad (6)$$

so that

$$MSE(D_p, t) = \mathbb{E}_{\mathbf{x}_t}[\text{tr}(\text{Cov}_p[\mathbf{x}|\mathbf{x}_t])] = \sigma_t^2 \mathbb{E}_{\mathbf{x}_t}[\text{tr}(\nabla D_p(\mathbf{x}_t))], \quad (7)$$

Thus, the Jacobian trace measures how much posterior uncertainty remains after observing \mathbf{x}_t : small traces indicate concentrated beliefs (InD), while large traces signal inflated uncertainty (OOD). Derivations are provided in Appendix (A.2).

Writing $\Sigma_t(\mathbf{x}_t) := \text{Cov}_p[\mathbf{x}|\mathbf{x}_t] = \sigma_t^2 \nabla D_p(\mathbf{x}_t)$, the covariance is symmetric positive semi-definite and admits the eigen-decomposition $\Sigma_t(\mathbf{x}_t) = \mathbf{U}_t \text{diag}(\lambda_1^t, \dots, \lambda_n^t) \mathbf{U}_t^T$, with nonnegative eigenvalues λ_k^t . Since $\text{tr}(\Sigma_t) = \sum_k \lambda_k^t$, the MSE corresponds to the sum of eigenvalues—the total uncertainty across all principal directions at noise level t :

$$MSE(D_p, t) = \mathbb{E}_{\mathbf{x}_t}[\text{tr}(\text{Cov}_p[\mathbf{x}|\mathbf{x}_t])] = \mathbb{E}_{\mathbf{x}_t}[\text{tr}(\Sigma_t(\mathbf{x}_t))] = \mathbb{E}_{\mathbf{x}_t} \left[\sum_{k=1}^n \lambda_k^t(\mathbf{x}_t) \right]. \quad (8)$$

For InD samples, the spectrum is compact with smaller leading eigenvalues, reflecting structured denoising aligned with the training data. For OOD samples, uncertainty spreads across multiple eigen-directions, inflating both the spectrum and the trace. This spectral inflation provides a quantitative signal of distribution shift. Figure 2 illustrates this effect: OOD samples exhibit consistently higher uncertainty, confirming the link between spectral inflation and distribution mismatch.

3.4 EigenScore as an OOD metric

While Prop.1 links distribution shift to excess denoising error, it requires two denoisers, whereas in practice we have only a single InD model. Combining Prop.1 with Eq. 7 implies that OOD inputs

exhibit inflated posterior covariance, which we can read from its eigenvalues. For each input \mathbf{x} and diffusion step t , we compute

$$m_t(\mathbf{x}) = \sum_{k=1}^K \lambda_k^t(\mathbf{x}_t), \quad \mathbf{x}_t = \mathbf{x} + \sigma_t \mathbf{z}, \quad \mathbf{z} \sim \mathcal{N}(0, \mathbf{I}), \quad (9)$$

the sum of the top- K eigenvalues across I noise realizations. These are aggregated (e.g., by mean, median, or full set) into $\bar{m}_t(\mathbf{x})$, yielding the EigenScore feature vector

$$\mathbf{M}(\mathbf{x}) = [\bar{m}_1(\mathbf{x}), \dots, \bar{m}_T(\mathbf{x})]^\top. \quad (10)$$

We normalize each coordinate using Z-scores with statistics (μ_t, σ_t) computed on training set $z_t(\mathbf{x}) = (\bar{m}_t(\mathbf{x}) - \mu_t)/\sigma_t$. The final OOD score is the sum of normalized coordinates, with the number of timesteps T tuned for efficiency on validation data.

Direct Jacobian evaluation is costly. Following [62], we estimate the top- K eigenvalues using a Jacobian-free subspace iteration. The method approximates Jacobian-vector products with finite differences of the denoiser $\mathbf{v}^+ \approx (\mathbf{D}(\mathbf{x}_t + c\mathbf{v}) - \mathbf{D}(\mathbf{x}_t - c\mathbf{v}))/2c$, where $c \ll 1$ is the linear approximation constant, \mathbf{v} is the current principle component, and \mathbf{v}^+ in the next principle component. We then orthogonalizes directions via QR. After a few iterations, eigenvalues are obtained as

$$\lambda_k^t(\mathbf{x}_t) \approx \frac{\sigma_t^2}{2c} \|\mathbf{D}(\mathbf{x}_t + c\mathbf{v}^k) - \mathbf{D}(\mathbf{x}_t - c\mathbf{v}^k)\|_2. \quad (11)$$

Full pseudo-code is given in App. B.1.

3.5 EigenScore vs. MSE: Capturing Structure Instead of Collapse

Eq. (4) and Prop. 1 show that distribution shift manifests as excess denoising error, measurable through the posterior covariance. However, scalar metrics such as MSE or score norms collapse this uncertainty into a single number, discarding how variance is distributed across directions. At high noise levels, this collapse is particularly problematic: many small eigenvalues are dominated by isotropic noise, obscuring class-specific structure. The following lemma formalizes this effect.

Lemma 1. *Let $p(\mathbf{x}_t) = p * \mathcal{N}(0, \sigma_t^2 \mathbf{I})$ denotes the noisy marginal in Eq. (3) and let $\Sigma_t(\mathbf{x}_t) = \sigma_t^2 (\mathbf{I} + \sigma_t^2 \nabla^2 \log p(\mathbf{x}_t))$ from Eq. (6). As $\sigma_t \rightarrow \infty$, $\|\nabla^2 \log p(\mathbf{x}_t)\| \rightarrow 0$ uniformly on compact sets. Hence*

$$\Sigma_t(\mathbf{x}_t) = \sigma_t^2 \mathbf{I} + o(\sigma_t^2),$$

so all eigenvalues satisfy $\lambda_k^t(\mathbf{x}_t) = \sigma_t^2 + o(\sigma_t^2)$.

Lemma 1 implies that the spectrum flattens under heavy Gaussian smoothing: all directions approach the same variance σ_t^2 , so low-variance components lose discriminative information. Consequently, MSE and score norms aggregate mostly isotropic noise, rather than meaningful structure (proof in App. A.4). To retain the informative structure, we focus on the dominant modes. Ky Fan’s theorem guarantees that the top- K eigenvalues capture the maximal variance among all K -dimensional projections:

Proposition 2 (Ky Fan’s theorem [63]). *Let $\Sigma_t(\mathbf{x}_t) \succeq 0$ have eigenvalues $\lambda_1^t \geq \dots \geq \lambda_n^t$ with eigenvectors forming $\mathbf{U}_t = [\mathbf{u}_1^t, \dots, \mathbf{u}_K^t]$. For any $K \in \{1, \dots, n\}$,*

$$\max_{\mathbf{V} \in \mathbb{R}^{n \times K}: \mathbf{V}^\top \mathbf{V} = \mathbf{I}_K} \text{tr}(\mathbf{V}^\top \Sigma_t(\mathbf{x}_t) \mathbf{V}) = \sum_{k=1}^K \lambda_k,$$

and a maximizer is $\mathbf{V}^* = [\mathbf{u}_1^t, \dots, \mathbf{u}_K^t]$.

By retaining only the top- K eigenvalues, EigenScore preserves the most informative uncertainty directions while discarding noise-dominated components. This explains its consistent advantage over MSE and score-based metrics. The choice of K is not dictated by theory, but reflects a practical trade-off between capturing discriminative information and computational efficiency (see App. A.5 for proof).

Table 1: *Main OOD detection results (AUROC). Comparison of EigenScore with likelihood-based, reconstruction-based, and diffusion-based baselines across multiple InD–OOD dataset pairings (CelebA, C10, C100, SVHN). **Best** and **second best** are highlighted. Note that EigenScore achieves the best average performance and is either best or second best in most settings.*

| InD OOD | CelebA vs. | | | C10 vs. | | | C100 vs. | | | SVHN vs. | | | Avg |
|--------------------------|--------------|--------------|--------------|--------------|--------------|--------------|--------------|--------------|--------------|--------------|--------------|--------------|--------------|
| | C10 | C100 | SVHN | C100 | SVHN | CelebA | C10 | CelebA | SVHN | C10 | C100 | CelebA | |
| DoS | 0.630 | 0.615 | 0.808 | 0.504 | 0.752 | 0.456 | 0.491 | 0.520 | 0.777 | 0.911 | 0.904 | 0.956 | 0.693 |
| TT | 0.676 | 0.655 | 0.773 | 0.558 | 0.714 | 0.469 | 0.538 | 0.464 | 0.648 | 0.957 | 0.961 | 0.994 | 0.701 |
| WAIC | 0.589 | 0.569 | 0.793 | 0.476 | 0.760 | 0.469 | 0.502 | 0.530 | 0.782 | 0.978 | 0.974 | 0.955 | 0.698 |
| <i>Diffusion-based</i> | | | | | | | | | | | | | |
| NLL | 0.507 | 0.671 | 0.753 | 0.558 | 0.545 | 0.599 | 0.480 | 0.484 | 0.481 | 0.635 | 0.660 | 0.636 | 0.584 |
| IC | 0.510 | 0.673 | 0.755 | 0.552 | 0.540 | 0.583 | 0.460 | 0.466 | 0.469 | 0.625 | 0.653 | 0.625 | 0.576 |
| DDPM-OOD | 0.922 | 0.928 | 0.992 | 0.618 | 0.944 | 0.642 | 0.462 | 0.496 | 0.870 | 0.963 | 0.972 | 0.996 | 0.817 |
| LMD | 0.886 | 0.848 | 0.950 | 0.601 | 0.821 | 0.834 | 0.569 | 0.595 | 0.748 | 0.780 | 0.749 | 0.872 | 0.771 |
| DiffPath (CelebA) | 1.000 | 1.000 | 0.964 | 0.554 | 0.729 | 0.885 | 0.475 | 0.887 | 0.724 | 0.919 | 0.941 | 0.328 | 0.784 |
| EigenScore (Ours) | 0.965 | 0.944 | 0.896 | 0.884 | 0.825 | 0.885 | 0.652 | 0.700 | 0.683 | 0.991 | 0.981 | 0.998 | 0.869 |

4 Experiments

We now evaluate the effectiveness of EigenScore for OOD detection. Specifically, we benchmark EigenScore across a suite of pairwise OOD detection tasks and compare its performance against state-of-the-art baselines.

Datasets. We evaluate OOD detection on standard image benchmarks commonly used with diffusion models: C10 [64], SVHN [65], C100 [64], and CelebA [66, 67]. For near-OOD tasks [68], we additionally include TinyImageNet [69]. Further details can be found in Appendix (B.4)

Baselines. We compare our method against several generative baselines for OOD detection, including Improved CD [70], DoS [46], TT [51], WAIC [5], NLL, IC, DDPM-OOD [3], LMD [36], DiffPath [35]. Details regarding the baselines can be found in Appendix (B.3).

4.1 Main Results

Table 1 reports AUROC results across all dataset pairs. EigenScore achieves the highest *average* performance across all settings and is best or second best on nearly every dataset pair. Its advantage is most pronounced in the challenging near–OOD regime (CIFAR-10 vs. CIFAR-100), where likelihood-based scores and trajectory metrics often fail. For example, EigenScore improves AUROC by up to 5% over the best diffusion-based baseline, consistent with our theoretical claim that retaining leading eigenvalues preserves discriminative structure.

On the near-OOD task [68] (C10 vs. C100/TinyImageNet), EigenScore continues to deliver strong separation, achieving higher average AUROC than other diffusion-based metrics in Table 2. In particular, while baselines such as NLL, IC, and WAIC (C10 vs. C100) struggle to distinguish the closely related distributions, EigenScore consistently maintains reliable performance, highlighting its robustness even under challenging near-OOD settings.

4.2 Ablations

We analyze how design choices influence EigenScore performance.

Table 2: *Near-OOD detection results (AUROC). We evaluate on semantically related datasets, including C10 vs. C100 and TinyImageNet, which are particularly challenging due to shared low-level statistics between InD and OOD samples. The **best** and **second best** methods are highlighted. EigenScore achieves the best average performance across both tasks, with a clear margin over prior diffusion-based approaches.*

| InD OOD | C10 vs. | | C100 vs. | | Avg |
|-------------------|--------------|--------------|--------------|--------------|--------------|
| | C100 | TinyImageNet | C10 | TinyImageNet | |
| DDPM-OOD | 0.618 | 0.570 | 0.462 | 0.457 | 0.527 |
| LMD | 0.601 | 0.592 | 0.569 | 0.558 | 0.580 |
| DiffPath | 0.554 | 0.993 | 0.475 | 0.995 | 0.754 |
| EigenScore | 0.884 | 0.973 | 0.652 | 0.888 | 0.849 |

Table 3: Ablation on timesteps T , repetitions I , and number of eigenvalues K . AUROC performance of EigenScore across InD–OOD dataset pairs.

| Timesteps | CelebA vs. | | | C10 vs. | | | C100 vs. | | | SVHN vs. | | | Avg |
|-----------------|--------------|--------------|--------------|--------------|--------------|--------------|--------------|--------------|--------------|--------------|--------------|--------------|--------------|
| | C10 | C100 | SVHN | C100 | SVHN | CelebA | C10 | CelebA | SVHN | C10 | C100 | CelebA | |
| 5 | 0.964 | 0.943 | 0.893 | 0.869 | 0.778 | 0.866 | 0.635 | 0.448 | 0.648 | 0.990 | 0.977 | 0.995 | 0.834 |
| 7 | 0.963 | 0.942 | 0.878 | 0.848 | 0.703 | 0.862 | 0.619 | 0.500 | 0.603 | 0.988 | 0.975 | 0.996 | 0.823 |
| 10 | 0.952 | 0.931 | 0.850 | 0.819 | 0.627 | 0.867 | 0.578 | 0.589 | 0.521 | 0.987 | 0.975 | 0.998 | 0.808 |
| Repetitions I | CelebA vs. | | | C10 vs. | | | C100 vs. | | | SVHN vs. | | | Avg |
| | C10 | C100 | SVHN | C100 | SVHN | CelebA | C10 | CelebA | SVHN | C10 | C100 | CelebA | |
| 5 | 0.959 | 0.940 | 0.885 | 0.863 | 0.773 | 0.857 | 0.635 | 0.455 | 0.649 | 0.990 | 0.977 | 0.995 | 0.832 |
| 10 | 0.962 | 0.942 | 0.889 | 0.867 | 0.776 | 0.864 | 0.635 | 0.450 | 0.650 | 0.990 | 0.978 | 0.995 | 0.833 |
| 15 | 0.962 | 0.942 | 0.891 | 0.869 | 0.778 | 0.866 | 0.635 | 0.447 | 0.649 | 0.990 | 0.977 | 0.994 | 0.833 |
| 20 | 0.964 | 0.943 | 0.893 | 0.869 | 0.778 | 0.866 | 0.635 | 0.448 | 0.648 | 0.990 | 0.977 | 0.995 | 0.834 |
| Eigenvalues K | CelebA vs. | | | C10 vs. | | | C100 vs. | | | SVHN vs. | | | Avg |
| | C10 | C100 | SVHN | C100 | SVHN | CelebA | C10 | CelebA | SVHN | C10 | C100 | CelebA | |
| 1 | 0.968 | 0.950 | 0.945 | 0.871 | 0.803 | 0.830 | 0.639 | 0.432 | 0.713 | 0.983 | 0.966 | 0.983 | 0.840 |
| 2 | 0.967 | 0.946 | 0.919 | 0.872 | 0.793 | 0.852 | 0.636 | 0.439 | 0.679 | 0.987 | 0.972 | 0.991 | 0.838 |
| 3 | 0.964 | 0.943 | 0.893 | 0.869 | 0.778 | 0.866 | 0.635 | 0.448 | 0.648 | 0.990 | 0.977 | 0.995 | 0.834 |

Number of timesteps. The parameter T determines how many points along the diffusion trajectory contribute to the score. Larger T includes more noise levels but increases computation and eventually saturates, since high noise merely lifts all eigenvalues uniformly (Lemma 1) without adding discriminative power. As shown in Table 3, even a small budget (e.g., $T=5$) achieves nearly the same AUROC as larger T , with only marginal improvements from denser schedules. This confirms that a compact subset of timesteps captures most of the useful information, balancing accuracy and efficiency.

Number of repetitions. The parameter I sets how many noise draws are averaged per timestep. Larger I reduces variance in the estimated eigenvalues and stabilizes OOD scores, but also increases runtime. As shown in Table 3, small values (e.g., $I=5$) are already sufficient, with only marginal gains beyond $I=15$. The results are reported with timesteps $t \in \{100, 150, 200, 250, 300\}$, mean aggregation, and $K=3$ eigenvalues.

Number of eigenvalues. The parameter K determines how many leading eigenvalues are aggregated at each timestep. Table 3 shows that $K=1$ achieves the best average performance, though in some settings $K=3$ yields slightly higher AUROC. This indicates that the bulk of discriminative information resides in the first few modes, consistent with Lemma 1. The results are reported with the same timestep schedule, mean aggregation, and $I=20$ repetitions.

EigenScore vs. MSE. EigenScore consistently outperforms MSE by retaining the spectral structure of posterior covariance rather than collapsing uncertainty into a single scalar. As shown in Table 4, this leads to higher AUROC across diverse dataset pairs. All experiments here use 20 repetitions, timesteps $t \in \{100, 150, 200, 250, 300\}$, and mean aggregation.

To further examine Lemma 1 and Prop. 2, we analyze the informativeness of individual eigenvalues across noise levels. Lemma 1 predicts that at larger t , eigenvalues converge toward σ_t^2 , diminishing their discriminative value. Figure 3 confirms this: AUROC with λ_1 decreases gradually as t increases, while λ_2 and λ_3 deteriorate more sharply. Prop. 2 further implies that the leading eigenvalues capture the most informative variance. Consistently, λ_1 provides the strongest OOD signal, followed by λ_2 and then λ_3 . These results highlight why focusing on dominant modes, as done in EigenScore, yields more stable and informative detection than scalarized measures such as MSE.

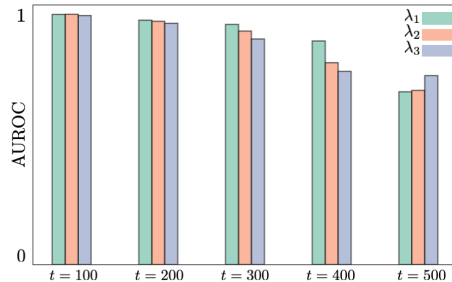


Figure 3: Ablation on eigenvalue informativeness across t . Performance declines with increasing noise, consistent with Lem. 1, while λ_1 retains the strongest OOD signal compared to λ_2 and λ_3 , supporting Prop. 2.

Table 4: Comparison of MSE vs. EigenScore. Average AUROC across all InD–OOD dataset pairs. EigenScore consistently outperforms MSE by leveraging spectral structure of the uncertainty.

| Method | CelebA vs. | | | C10 vs. | | | C100 vs. | | | SVHN vs. | | | Avg |
|------------|--------------|--------------|--------------|--------------|--------------|--------------|--------------|--------------|--------------|--------------|--------------|--------------|--------------|
| | C10 | C100 | SVHN | C100 | SVHN | CelebA | C10 | CelebA | SVHN | C10 | C100 | CelebA | |
| MSE | 0.804 | 0.783 | 0.220 | 0.629 | 0.184 | 0.841 | 0.552 | 0.675 | 0.147 | 0.994 | 0.994 | 1.000 | 0.652 |
| EigenScore | 0.964 | 0.943 | 0.893 | 0.869 | 0.778 | 0.866 | 0.635 | 0.448 | 0.648 | 0.990 | 0.977 | 0.995 | 0.834 |

5 Conclusion

We introduced EigenScore, a principled OOD detection method for diffusion models that leverages the spectral structure of denoising uncertainty. By linking KL divergence to excess denoising error and showing that posterior covariance inflation consistently signals distribution shift, EigenScore offers both theoretical justification and strong empirical performance. Across diverse benchmarks, EigenScore consistently outperformed likelihood-based and score-norm methods, with particularly robust gains in near-OOD settings where traditional approaches fail. Ablation studies further confirmed that most discriminative information lies in the leading eigenvalues at moderate noise levels, validating our spectral perspective.

Limitations

Despite its strengths, our approach has several limitations. First, EigenScore only leverages a subset of the information available in diffusion models: we use the eigenvalues of the posterior covariance but discard eigenvector structure, which may contain additional discriminative cues. Moreover, we compute features at a limited set of timesteps rather than across the full diffusion trajectory, potentially overlooking temporal dynamics of uncertainty. Second, our framework focuses on the magnitude of eigenvalues, but does not explicitly exploit their rate of change across eigenvalues, which itself may differ systematically between InD and OOD inputs and could serve as a detection signal.

References

- [1] J. Yang, K. Zhou, Y. Li, and Z. Liu, “Generalized Out-of-Distribution Detection: A Survey”, in *Int. J. Computer Vision*, 2024.
- [2] H. Zhang, H. Singh, M. Ghassemi, and S. Joshi, ““Why Did the Model Fail?”: Attributing Model Performance Changes to Distribution Shifts”, in *Proc. ICML*, 2023.
- [3] M. S. Graham, W. H. Pinaya, P.-D. Tudosiu, P. Nachev, S. Ourselin, and J. Cardoso, “Denoising Diffusion Models for Out-of-Distribution Detection”, in *Proc. CVPR Workshops*, June 2023.
- [4] D. Hendrycks and K. Gimpel, “A Baseline for Detecting Misclassified and Out-of-Distribution Examples in Neural Networks”, in *Proc. ICLR*, 2017.
- [5] H. Choi, E. Jang, and A. A. Alemi, “WAIC, but Why? Generative Ensembles for Robust Anomaly Detection,” *arXiv:1810.01392*, 2018.
- [6] X. Wang and L. Aitchison, “Bayesian OOD Detection with Aleatoric Uncertainty and Outlier Exposure”, in *Proc. Adv. Approx. Bayes. Infer.*, 2021.
- [7] B. Charpentier, D. Zügner, and S. Günnemann, “Posterior network: Uncertainty Estimation without OOD Samples via Density-based Pseudo-counts”, in *Proc. NeurIPS*, 2020.
- [8] S. Regmi, B. Panthi, Y. Ming, P. K. Gyawali, D. Stoyanov, and B. Bhattarai, “Reweightood: Loss Reweighting for Distance-based OOD Detection”, in *Proc. CVPR*, 2024.
- [9] P. Colombo, E. Dadalto, G. Staerman, N. Noiry, and P. Piantanida, “Beyond Mahalanobis Distance for Textual OOD Detection”, in *Proc. NeurIPS*, 2022.
- [10] K. Lee, K. Lee, H. Lee, and J. Shin, “A Simple Unified Framework for Detecting Out-of-Distribution Samples and Adversarial Attacks,” *Proc. NeurIPS*, vol. 31, 2018.
- [11] W. Huang, H. Wang, J. Xia, C. Wang, and J. Zhang, “Density-driven Regularization for Out-of-Distribution Detection”, in *Proc. NeurIPS*, 2022.
- [12] N. Kumar, S. Šegvić, A. Eslami, and S. Gumhold, “Normalizing Flow Based Feature Synthesis for Outlier-aware Object Detection”, in *Proc. CVPR*, 2023.
- [13] W. Liu, X. Wang, J. Owens, and Y. Li, “Energy-based Out-of-Distribution Detection”, in *Proc. NeurIPS*, 2020.
- [14] E. Nalisnick, A. Matsukawa, Y. Teh, D. Gorur, and B. Lakshminarayanan, “Do Deep Generative Models Know What They Don’t Know?”, in *Proc. ICLR*, 2019.
- [15] W. Wang, X. Lin, F. Feng, X. He, M. Lin, and T.-S. Chua, “Causal Representation Learning for Out-of-Distribution Recommendation”, in *Proc. ACM Web Conf.*, 2022.
- [16] S. Seifi, D. O. Reino, N. Chumerin, and R. Aljundi, “OOD Aware Supervised Contrastive Learning”, in *Proc. WACV*, 2024.
- [17] D. Hendrycks, M. Mazeika, S. Kadavath, and D. Song, “Using Self-supervised Learning Can Improve Model Robustness and Uncertainty”, in *Proc. NeurIPS*, 2019.
- [18] J. Tack, S. Mo, J. Jeong, and J. Shin, “Csi: Novelty Detection via Contrastive Learning on Distributionally Shifted Instances”, in *Proc. NeurIPS*, 2020.
- [19] P. W. Koh and et. al, “WILDS: A Benchmark of in-the-Wild Distribution Shifts”, in *Proc. ICML*, 2021.
- [20] M. Salehi, H. Mirzaei, D. Hendrycks, Y. Li, M. Rohban, M. Sabokrou, et al., “A Unified Survey on Anomaly, Novelty, Open-Set, and Out of-Distribution Detection: Solutions and Future Challenges,” *TMLR*, 2022.
- [21] J. Ho, A. Jain, and P. Abbeel, “Denoising Diffusion Probabilistic Models”, in *Proc. NeurIPS*, 2020.
- [22] Y. Song, J. Sohl-Dickstein, D. P. Kingma, A. Kumar, S. Ermon, and B. Poole, “Score-Based Generative Modeling through Stochastic Differential Equations”, in *Proc. ICLR*, 2020.
- [23] A. Vahdat, K. Kreis, and J. Kautz, “Score-based Generative Modeling in Latent Space”, in *Proc. NeurIPS*, 2021.
- [24] P. Dhariwal and A. Nichol, “Diffusion Models Beat GANs on Image Synthesis”, in *Proc. NeurIPS*, 2021.

- [25] R. Rombach, A. Blattmann, D. Lorenz, P. Esser, and B. Ommer, “High-resolution Image Synthesis with Latent Diffusion Models”, in *Proc. CVPR*, 2022.
- [26] T. Karras, M. Aittala, T. Aila, and S. Laine, “Elucidating the Design Space of Diffusion-Based Generative Models”, in *Proc. NeurIPS*, 2022.
- [27] H. Chung, J. Kim, M. T. Mccann, M. L. Klasky, and J. C. Ye, “Diffusion Posterior Sampling for General Noisy Inverse Problems”, in *Proc. ICLR*, 2023.
- [28] E. Adib, A. Fernandez, F. Afghah, and J. J. Prevost, “Synthetic ECG Signal Generation using Probabilistic Diffusion Models,” *IEEE Access*, vol. 11, pp. 75818–75828, 2023.
- [29] G. Daras, H. Chung, C.-H. Lai, Y. Mitsufuji, J. C. Ye, P. Milanfar, A. G. Dimakis, and M. Delbracio, “A Survey on Diffusion Models for Inverse Problems,” *arXiv:2410.00083*, 2024.
- [30] F.-A. Croitoru, V. Hondru, R. T. Ionescu, and M. Shah, “Diffusion Models in Vision: A survey,” *IEEE Trans. PAMI*, vol. 45, no. 9, pp. 10850–10869, 2023.
- [31] X. Li, Y. Ren, X. Jin, C. Lan, X. Wang, W. Zeng, X. Wang, and Z. Chen, “Diffusion Models for Image Restoration and Enhancement—A Comprehensive Survey,” *arXiv e-prints*, pp. arXiv–2308, 2023.
- [32] A. Kazerouni, E. Aghdam, M. Heidari, R. Azad, M. Fayyaz, I. Hacihaliloglu, and D. Merhof, “Diffusion Models in Medical Imaging: A Comprehensive Survey,” *Med. Image Anal.*, vol. 88, pp. 102846–102846, 2023.
- [33] R. Gao, C. Zhao, L. Hong, and Q. Xu, “DIFFGUARD: Semantic Mismatch-Guided Out-of-Distribution Detection Using Pre-Trained Diffusion Models”, in *Proc. ICCV*, 2023.
- [34] Z. He, C. Zhao, M. Shao, Y. Lin, D. Li, and Q. Tian, “GDDA: Semantic OOD Detection on Graphs under Covariate Shift via Score-based Diffusion Models”, in *Proc. ICASSP*, 2025.
- [35] A. Heng, H. Soh, et al., “Out-of-distribution Detection with a Single Unconditional Diffusion Model”, in *Proc. NeurIPS*, 2024.
- [36] Z. Liu, J. P. Zhou, Y. Wang, and K. Q. Weinberger, “Unsupervised Out-of-distribution Detection with Diffusion Inpainting”, in *Proc. ICML*, 2023.
- [37] S. Choi, H. Lee, H. Lee, and M. Lee, “Projection Regret: Reducing Background Bias for Novelty Detection via Diffusion Models”, in *Proc. NeurIPS*, 2023.
- [38] H. Robbins, “An Empirical Bayes Approach to Statistics”, in *Proc Third Berkeley Symposium on Mathematical Statistics and Probability*, 1956.
- [39] K. Miyasawa, “An Empirical Bayes Estimator of the Mean of a Normal Population,” *Bull. Inst. Internat. Statist.*, vol. 38, pp. 181–188, 1961.
- [40] P. Vincent, “A Connection Between Score Matching and Denoising Autoencoders,” *Neural Computation*, vol. 23, no. 7, pp. 1661–1674, 2011.
- [41] M. Raphan and E. P. Simoncelli, “Least Squares Estimation without Priors or Supervision,” *Neural Computation*, vol. 23, no. 2, pp. 374–420, Feb 2011.
- [42] Y. Song and S. Ermon, “Generative Modeling by Estimating Gradients of the Data Distribution”, in *Proc. NeurIPS*, 2019.
- [43] L. Yang, Z. Zhang, Y. Song, S. Hong, R. Xu, Y. Zhao, W. Zhang, B. Cui, and M. H. Yang, “Diffusion Models: A Comprehensive Survey of Methods and Applications,” *ACM Comput. Surv.*, vol. 56, no. 4, pp. 105, 2023.
- [44] T. Salimans, A. Karpathy, X. Chen, and D. P. Kingma, “PixelCNN++: Improving the PixelCNN with Discretized Logistic Mixture Likelihood and Other Modifications”, in *Proc. ICLR*, 2017.
- [45] D. P. Kingma and P. Dhariwal, “Glow: Generative Flow with Invertible 1x1 Convolutions”, in *Proc. NeurIPS*, 2018.
- [46] W. Morningstar, C. Ham, A. Gallagher, B. Lakshminarayanan, A. Alemi, and J. Dillon, “Density of States Estimation for Out of Distribution Detection”, in *Proc. AISTATS*, 2021.
- [47] Y. Ding, A. Aleksandrauskas, A. Ahmadian, J. Unger, F. Lindsten, and G. Eilertsen, “Revisiting Likelihood-Based Out-of-Distribution Detection by Modeling Representations”, in *arXiv:2504.07793*, 2025.

- [48] P. Kirichenko, P. Izmailov, and A. G. Wilson, “Why Normalizing Flows Fail to Detect Out-of-distribution Data”, in *Proc. NeurIPS*, 2020.
- [49] J. Ren, P. J. Liu, E. A. Fertig, J. R. Snoek, R. Poplin, M. DePristo, J. Dillon, and B. Lakshminarayanan, “Likelihood Ratios for Out-of-Distribution Detection”, in *Proc. NeurIPS*, 2019.
- [50] J. Serrà, D. Álvarez, V. Gómez, O. Slizovskaia, J. F. Núñez, and J. Luque, “Input Complexity and Out-of-distribution Detection with Likelihood-based Generative Models”, in *Proc. ICLR*, 2019.
- [51] E. Nalisnick, A. Matsukawa, Y. W. Teh, and B. Lakshminarayanan, “Detecting Out-of-Distribution Inputs to Deep Generative Models Using Typicality”, in *arXiv:1906.02994*, 2019.
- [52] V. Livernoche, V. Jain, Y. Hezaveh, and S. Ravanbakhsh, “On Diffusion Modeling for Anomaly Detection”, in *Proc. ICLR*, 2024.
- [53] C. Zhou and R. C. Paffenroth, “Anomaly Detection with Robust Deep Autoencoders”, in *Proc. ACM SIGKDD Int. Conf. Knowl. Discov. Data Min.*, 2017.
- [54] T. Schlegl, P. Seeböck, S. M. Waldstein, G. Langs, and U. Schmidt-Erfurth, “f-AnoGAN: Fast Unsupervised Anomaly Detection with Generative Adversarial Networks,” *Med. Image Anal.*, vol. 54, pp. 30–44, 2019.
- [55] T. Denouden, R. Salay, K. Czarnecki, V. Abdelzad, B. Phan, and S. Vernekar, “Improving Reconstruction Autoencoder Out-of-distribution Detection with Mahalanobis Distance,” *arXiv:1812.02765*, 2018.
- [56] L. Bergman and Y. Hoshen, “Classification-Based Anomaly Detection for General Data”, in *Proc. ICLR*, 2020.
- [57] A. Ahmadian and F. Lindsten, “Likelihood-free Out-of-Distribution Detection with Invertible Generative Models”, in *Proc. IJCAI*, 2021.
- [58] Z. Xiao, Q. Yan, and Y. Amit, “Likelihood Regret: An Out-of-distribution Detection Score for Variational Auto-encoder”, in *Proc. NeurIPS*, 2020.
- [59] Y. Song, C. Durkan, I. Murray, and S. Ermon, “Maximum Likelihood Training of Score-based Diffusion Models”, in *Proc. NeurIPS*, 2021.
- [60] Z. Kadkhodaie, F. Guth, E. P. Simoncelli, and S. Mallat, “Generalization in Diffusion Models Arises from Geometry-adaptive Harmonic Representations”, in *Proc. ICLR*, 2024.
- [61] S. Shoushtari, E. P. Chandler, Y. Wang, M. S. Asif, and U. S. Kamilov, “Unsupervised Detection of Distribution Shift in Inverse Problems using Diffusion Models,” *arXiv:2505.11482*, 2025.
- [62] H. Manor and T. Michaeli, “On the Posterior Distribution in Denoising: Application to Uncertainty Quantification”, in *Proc. ICLR*, 2024.
- [63] K. Fan, “On a Theorem of Weyl Concerning Eigenvalues of Linear Transformations: II,” *Proceedings of the National Academy of Sciences*, vol. 36, no. 1, pp. 31–35, 1950.
- [64] A. Krizhevsky, “Learning Multiple Layers of Features from Tiny Images,” Tech. Rep., University of Toronto, 2009, Technical report.
- [65] Y. Netzer, T. Wang, A. Coates, B. Bissacco, B. Wu, and A. Y. Ng, “Reading Digits in Natural Images with Unsupervised Feature Learning”, in *Neurips Workshop on Deep Learning and Unsupervised Feature Learning*, 2011.
- [66] Z. Liu, P. Luo, X. Wang, and X. Tang, “CelebFaces Attributes (CelebA) Dataset,” 2015.
- [67] Z. Liu, P. Luo, X. Wang, and X. Tang, “Deep Learning Face Attributes in the Wild”, in *Proc. ICCV*, 2015.
- [68] J. Yang, P. Wang, D. Zou, Z. Zhou, K. Ding, W. Peng, H. Wang, G. Chen, B. Li, Y. Sun, et al., “OpenOOD: Benchmarking generalized out-of-distribution detection,” *Proc. NeurIPS*, vol. 35, pp. 32598–32611, 2022.
- [69] Y. Le and X. Yang, “Tiny ImageNet Visual Recognition Challenge,” 2015, Accessed: YYYY-MM-DD.
- [70] Y. Du, S. Li, J. Tenenbaum, and I. Mordatch, “Improved Contrastive Divergence Training of Energy-Based Models”, in *Proc. ICML*, 2021.

A Proofs

A.1 Connecting KL divergence with Denoising Error

Eq. (4) is inspired from the work of [59] [Theorem 1] and [61] [Theorem 1], where KL divergence between two distribution is stated in terms of fisher divergence:

$$D_{\text{KL}}(p \parallel q) = \int_0^\infty \mathbb{E}_{\mathbf{x}, \mathbf{x}_t} \left[\|\nabla \log p(\mathbf{x}_t) - \nabla \log q(\mathbf{x}_t)\|_2^2 \right] \sigma_t dt. \quad (12)$$

By using the Tweedie's formula from Eq. (2)

$$D_p(\mathbf{x}_t) = \mathbb{E}_p[\mathbf{x}|\mathbf{x}_t] = \mathbf{x}_t + \sigma_t^2 \nabla \log p(\mathbf{x}_t),$$

and replacing the score functions for distributions p and q with their corresponding MMSE estimators, we have:

$$\begin{aligned} D_{\text{KL}}(p \parallel q) &= \int_0^\infty \mathbb{E}_{\mathbf{x}, \mathbf{x}_t} \left[\|\mathbb{E}_p[\mathbf{x}|\mathbf{x}_t] - \mathbb{E}_q[\mathbf{x}|\mathbf{x}_t]\|_2^2 \right] \sigma_t^{-3} dt \\ &= \int_0^\infty \left\{ \mathbb{E}_{\mathbf{x}, \mathbf{x}_t} \left[\|\mathbf{x} - \mathbb{E}_q[\mathbf{x}|\mathbf{x}_t]\|_2^2 \right] - \mathbb{E}_{\mathbf{x}, \mathbf{x}_t} \left[\|\mathbf{x} - \mathbb{E}_p[\mathbf{x}|\mathbf{x}_t]\|_2^2 \right] \right\} \sigma_t^{-3} dt, \end{aligned} \quad (13)$$

where in the second line, we used the following decomposition:

$$\begin{aligned} \mathbb{E}_{\mathbf{x}, \mathbf{x}_t} \left[\|\mathbf{x} - \mathbb{E}_q[\mathbf{x}|\mathbf{x}_t]\|_2^2 \right] &= \mathbb{E}_{\mathbf{x}, \mathbf{x}_t} \left[\|\mathbf{x} - \mathbb{E}_p[\mathbf{x}|\mathbf{x}_t] + \mathbb{E}_p[\mathbf{x}|\mathbf{x}_t] - \mathbb{E}_q[\mathbf{x}|\mathbf{x}_t]\|_2^2 \right] \\ &= \mathbb{E}_{\mathbf{x}, \mathbf{x}_t} \left[\|\mathbf{x} - \mathbb{E}_p[\mathbf{x}|\mathbf{x}_t]\|_2^2 \right] + \mathbb{E}_{\mathbf{x}, \mathbf{x}_t} \left[\|\mathbb{E}_p[\mathbf{x}|\mathbf{x}_t] - \mathbb{E}_q[\mathbf{x}|\mathbf{x}_t]\|_2^2 \right] \\ &\quad + 2\mathbb{E}_{\mathbf{x}, \mathbf{x}_t} \left[(\mathbf{x} - \mathbb{E}_p[\mathbf{x}|\mathbf{x}_t])^\top (\mathbb{E}_p[\mathbf{x}|\mathbf{x}_t] - \mathbb{E}_q[\mathbf{x}|\mathbf{x}_t]) \right] \\ &= \mathbb{E}_{\mathbf{x}, \mathbf{x}_t} \left[\|\mathbf{x} - \mathbb{E}_p[\mathbf{x}|\mathbf{x}_t]\|_2^2 \right] + \mathbb{E}_{\mathbf{x}, \mathbf{x}_t} \left[\|\mathbb{E}_p[\mathbf{x}|\mathbf{x}_t] - \mathbb{E}_q[\mathbf{x}|\mathbf{x}_t]\|_2^2 \right], \end{aligned}$$

where in the last equality, we used the fact that

$$\mathbb{E}_{\mathbf{x}, \mathbf{x}_t} \left[(\mathbf{x} - \mathbb{E}_p[\mathbf{x}|\mathbf{x}_t])^\top (\mathbb{E}_p[\mathbf{x}|\mathbf{x}_t] - \mathbb{E}_q[\mathbf{x}|\mathbf{x}_t]) \right] = 0, \quad \text{where } \mathbf{x} \sim p(\mathbf{x}) \text{ and } \mathbf{x}_t \sim p(\mathbf{x}_t).$$

By replacing the result of this equation into Eq. (13)

$$\begin{aligned} \mathbb{E}_{\mathbf{x}, \mathbf{x}_t} \left[\|\mathbb{E}_p[\mathbf{x}|\mathbf{x}_t] - \mathbb{E}_q[\mathbf{x}|\mathbf{x}_t]\|_2^2 \right] &= \mathbb{E}_{\mathbf{x}, \mathbf{x}_t} \left[\|\mathbf{x} - \mathbb{E}_q[\mathbf{x}|\mathbf{x}_t]\|_2^2 \right] - \mathbb{E}_{\mathbf{x}, \mathbf{x}_t} \left[\|\mathbf{x} - \mathbb{E}_p[\mathbf{x}|\mathbf{x}_t]\|_2^2 \right] \\ &= \text{MSE}(D_q, t) - \text{MSE}(D_p, t). \end{aligned}$$

A.2 Connecting MSE of Denoising to Covariance

We assume that MMSE estimator D_p is an optimal denoiser trained on images sampled from data distribution $p(\mathbf{x})$. Consequently, the MSE for this operator is defined as

$$\begin{aligned} \text{MSE}(D_p, t) &= \mathbb{E}_{\mathbf{x}, \mathbf{x}_t} \left[\|\mathbf{x} - \mathbb{E}_p[\mathbf{x}|\mathbf{x}_t]\|_2^2 \right] = \mathbb{E}_{\mathbf{x}} \left[\mathbb{E}_{\mathbf{x}_t} \left[\text{tr}(\mathbf{x} - \mathbb{E}_p[\mathbf{x}|\mathbf{x}_t])(\mathbf{x} - \mathbb{E}_p[\mathbf{x}|\mathbf{x}_t])^\top | \mathbf{x}_t \right] \right] \\ &= \mathbb{E}_{\mathbf{x}} \left[\text{tr Cov}_p[\mathbf{x}|\mathbf{x}_t] \right], \end{aligned}$$

where the first equality follows from the definition of MSE using the MMSE estimator $D_p(\mathbf{x}_t) = \mathbb{E}_p[\mathbf{x}|\mathbf{x}_t]$, and the second equality applies the law of total expectation along with the identity $\|\mathbf{v}\|_2^2 = \text{tr}(\mathbf{v}\mathbf{v}^\top)$. In the last equality, we used the fact that the inner expectation corresponds to the conditional covariance matrix $\text{Cov}[\mathbf{x}|\mathbf{x}_t]$, whose trace gives the expected squared error. From Theorem 1 of [62], we have

$$\text{Cov}_p[\mathbf{x}|\mathbf{x}_t] = \sigma_t^2 \nabla D_p(\mathbf{x}_t) \approx \sum_{k=1}^K \lambda_k^t(\mathbf{x}_t) \mathbf{u}_k \mathbf{u}_k^\top, \quad (14)$$

where ∇D_p is the Jacobian, assumed to be positive semi-definite and symmetric. We approximate the Jacobian matrix using the top K eigenvalues $\lambda_1, \dots, \lambda_K$, and their corresponding eigenvectors $\mathbf{u}_1, \dots, \mathbf{u}_K$ which is a low-rank approximation of the full covariance matrix based on its spectral decomposition of symmetric positive semi-definite matrices. By retaining only the top $K < n$ terms in this expansion, we obtain a rank- K approximation of the covariance, capturing most of its variance while reducing dimensionality and computation. The trace of this approximate covariance is then given by

$$\text{tr}(\text{Cov}_p[\mathbf{x}|\mathbf{x}_t]) \approx \sum_{k=1}^K \lambda_k^t(\mathbf{x}_t), \quad (15)$$

since each term $\mathbf{u}_k \mathbf{u}_k^\top$ is a rank-one projection matrix with unit trace. This expression allows us to estimate the total variance (or the MSE) using only the top eigenvalues, under the assumption that the remaining eigenvalues contribute negligibly. Consequently, we have:

$$\text{MSE}(D_p, t) = \mathbb{E}_{\mathbf{x}} \left[\text{tr} \text{Cov}_p[\mathbf{x}|\mathbf{x}_t] \right] = \sigma_t^2 \sum_{k=1}^K \lambda_k^t(\mathbf{x}_t). \quad (16)$$

A.3 Miyasawa Relationship

The connection between MMSE estimation under Gaussian noise and the score function was first established in [39] and later generalized in [41]. For completeness, we provide a derivation here.

Let $\mathbf{x}_t = \mathbf{x} + \mathbf{z}$, denote a noisy observation of $\mathbf{x} \sim p(\mathbf{x})$, where $\mathbf{z} \sim \mathcal{N}(0, \sigma_t^2 \mathbf{I})$, and define $p(\mathbf{x}_t|\mathbf{x})$ as the Gaussian likelihood. The marginal distribution of \mathbf{y} is given by:

$$p(\mathbf{x}_t) = \int p(\mathbf{x}) p(\mathbf{x}_t|\mathbf{x}) d\mathbf{x}.$$

To derive the score function $\nabla_{\mathbf{x}_t} \log p(\mathbf{x}_t)$, we differentiate the log-marginal using the identity $\nabla h(\mathbf{x}_t) = h(\mathbf{x}_t) \nabla \log h(\mathbf{x}_t)$:

$$\begin{aligned} \nabla_{\mathbf{x}_t} \log p(\mathbf{x}_t) &= \int p(\mathbf{x}) p(\mathbf{x}_t|\mathbf{x}) \nabla_{\mathbf{x}_t} \log p(\mathbf{x}_t|\mathbf{x}) d\mathbf{x} \Big/ p(\mathbf{x}_t) \\ &= \int p(\mathbf{x}|\mathbf{x}_t) \nabla_{\mathbf{x}_t} \log p(\mathbf{x}_t|\mathbf{x}) d\mathbf{x} \\ &= \mathbb{E} [\nabla_{\mathbf{x}_t} \log p(\mathbf{x}_t|\mathbf{x}) \mid \mathbf{x}_t], \end{aligned}$$

which can be interpreted as a chain rule applied to score functions rather than densities.

Next, we compute the Hessian $\nabla^2 \log p(\mathbf{x}_t)$. Differentiating again:

$$\nabla^2 \log p(\mathbf{x}_t) = \int p(\mathbf{x}|\mathbf{x}_t) (\nabla_{\mathbf{x}_t} \log p(\mathbf{x}|\mathbf{x}_t) \nabla_{\mathbf{x}_t} \log p(\mathbf{x}_t|\mathbf{x})^\top + \nabla_{\mathbf{x}_t}^2 \log p(\mathbf{x}_t|\mathbf{x})) d\mathbf{x}.$$

Using Bayes' rule:

$$\log p(\mathbf{x}|\mathbf{x}_t) = \log p(\mathbf{x}_t|\mathbf{x}) + \log p(\mathbf{x}) - \log p(\mathbf{x}_t),$$

and differentiating with respect to \mathbf{y} , we obtain:

$$\nabla_{\mathbf{x}_t} \log p(\mathbf{x}|\mathbf{x}_t) = \nabla_{\mathbf{x}_t} \log p(\mathbf{x}_t|\mathbf{x}) - \nabla \log p(\mathbf{x}_t).$$

Substituting this into the previous expression yields:

$$\begin{aligned} \nabla^2 \log p(\mathbf{x}_t) &= \int p(\mathbf{x}|\mathbf{x}_t) ((\nabla_{\mathbf{x}_t} \log p(\mathbf{x}_t|\mathbf{x}) - \nabla \log p(\mathbf{x}_t)) \nabla_{\mathbf{x}_t} \log p(\mathbf{x}_t|\mathbf{x})^\top + \nabla_{\mathbf{x}_t}^2 \log p(\mathbf{x}_t|\mathbf{x})) d\mathbf{x} \\ &= \mathbb{E} [(\nabla_{\mathbf{x}_t} \log p(\mathbf{x}_t|\mathbf{x}) - \nabla \log p(\mathbf{x}_t)) \nabla_{\mathbf{x}_t} \log p(\mathbf{x}_t|\mathbf{x})^\top \mid \mathbf{x}_t] + \mathbb{E} [\nabla_{\mathbf{x}_t}^2 \log p(\mathbf{x}_t|\mathbf{x}) \mid \mathbf{x}_t] \\ &= \text{Cov} [\nabla_{\mathbf{x}_t} \log p(\mathbf{x}_t|\mathbf{x}) \mid \mathbf{x}_t] + \mathbb{E} [\nabla_{\mathbf{x}_t}^2 \log p(\mathbf{x}_t|\mathbf{x}) \mid \mathbf{x}_t]. \end{aligned}$$

Now, since $p(\mathbf{x}_t|\mathbf{x})$ is Gaussian with variance $\sigma_t^2 \mathbf{I}$, we have:

$$\begin{aligned}\log p(\mathbf{x}_t|\mathbf{x}) &= -\frac{1}{2\sigma_t^2} \|\mathbf{x}_t - \mathbf{x}\|^2 + \text{const}, \\ \nabla_{\mathbf{x}_t} \log p(\mathbf{x}_t|\mathbf{x}) &= -\frac{1}{\sigma_t^2} (\mathbf{x}_t - \mathbf{x}), \\ \nabla_{\mathbf{x}_t}^2 \log p(\mathbf{x}_t|\mathbf{x}) &= -\frac{1}{\sigma_t^2} \mathbf{I}.\end{aligned}$$

Plugging into the previous results gives the Miyasawa identities:

$$\nabla \log p(\mathbf{x}_t) = \frac{1}{\sigma_t^2} (\mathbb{E}[\mathbf{x} | \mathbf{x}_t] - \mathbf{x}_t), \quad (17)$$

$$\nabla^2 \log p(\mathbf{x}_t) = \frac{1}{\sigma_t^4} \text{Cov}[\mathbf{x} | \mathbf{x}_t] - \frac{1}{\sigma_t^2} \mathbf{I}. \quad (18)$$

Rearranging, we recover both the posterior mean and posterior covariance in terms of the score and its Hessian:

$$\mathbb{E}[\mathbf{x} | \mathbf{x}_t] = \mathbf{x}_t + \sigma_t^2 \nabla \log p(\mathbf{x}_t), \quad (19)$$

$$\text{Cov}[\mathbf{x} | \mathbf{x}_t] = \sigma_t^2 (\mathbf{I} + \sigma_t^2 \nabla^2 \log p(\mathbf{x}_t)). \quad (20)$$

Finally, the optimal denoising error is given by the expected trace of the posterior covariance:

$$\mathbb{E} [\|\mathbf{x} - \mathbb{E}[\mathbf{x} | \mathbf{x}_t]\|^2] = \mathbb{E} [\text{tr Cov}[\mathbf{x} | \mathbf{x}_t]].$$

A.4 Proof of Lemma 1.

Lemma 1 *Let $p(\mathbf{x}_t) = p * \mathcal{N}(0, \sigma_t^2 \mathbf{I})$ denotes the noisy marginal distribution in Eq. (3) and $\Sigma_t(\mathbf{x}_t) = \sigma_t^2 (\mathbf{I} + \sigma_t^2 \nabla^2 \log p(\mathbf{x}_t))$ from Miyasawa (Eq. (6)). As $\sigma_t \rightarrow \infty$, $\|\nabla^2 \log p(\mathbf{x}_t)\| \rightarrow 0$ uniformly on compact sets. Hence*

$$\Sigma_t(\mathbf{x}_t) = \sigma_t^2 \mathbf{I} + o(\sigma_t^2),$$

so all eigenvalues satisfy $\lambda_k^t(\mathbf{x}_t) = \sigma_t^2 + o(\sigma_t^2)$.

Proof. Let G_{σ_t} denotes the Gaussian density function with standard deviation $\sigma_t \geq 0$. Then, we have

$$p(\mathbf{x}_t) = \int p(\mathbf{x}_t|\mathbf{x}) p(\mathbf{x}) d\mathbf{x} = \int G_{\sigma_t}(\mathbf{x}_t - \mathbf{x}) p(\mathbf{x}) d\mathbf{x}, \quad (21)$$

Differentiation under the integral yields

$$\nabla G_{\sigma}(z) = -\frac{z}{\sigma^2} G_{\sigma}(z), \quad \nabla^2 G_{\sigma}(z) = \left(\frac{zz^{\top}}{\sigma^4} - \frac{\mathbf{I}}{\sigma^2} \right) G_{\sigma}(z). \quad (22)$$

Hence

$$\nabla_{\mathbf{x}_t} p(\mathbf{x}_t) = \int \nabla G_{\sigma_t}(\mathbf{x}_t - \mathbf{x}) p(\mathbf{x}) d\mathbf{x}, \quad \nabla_{\mathbf{x}_t}^2 p(\mathbf{x}_t) = \int \nabla^2 G_{\sigma_t}(\mathbf{x}_t - \mathbf{x}) p(\mathbf{x}) d\mathbf{x}. \quad (23)$$

Fix a compact set $K \subset \mathbb{R}^d$. Using Cauchy–Schwarz and that p has finite second moment, one obtains bounds of the form

$$\frac{\|\nabla p(\mathbf{x}_t)\|}{p(\mathbf{x}_t)} \leq \frac{C_1}{\sigma_t}, \quad \frac{\|\nabla^2 p(\mathbf{x}_t)\|}{p(\mathbf{x}_t)} \leq \frac{C_2}{\sigma_t^2}, \quad \forall \mathbf{x} \in K, \quad (24)$$

for constants C_1, C_2 independent of σ_t . Consequently,

$$\nabla^2 \log p(\mathbf{x}_t) = \frac{\nabla^2 p(\mathbf{x}_t)}{p(\mathbf{x}_t)} - \frac{\nabla p(\mathbf{x}_t) \nabla p(\mathbf{x}_t)^{\top}}{p(\mathbf{x}_t)^2} \quad (25)$$

satisfies

$$\|\nabla^2 \log p(\mathbf{x}_t)\| \leq \frac{C_2}{\sigma_t^2} + \frac{C_1^2}{\sigma_t^2} = O\left(\frac{1}{\sigma_t^2}\right), \quad (26)$$

uniformly on K . Thus $\sigma_t^2 \nabla^2 \log p(\mathbf{x}_t) \rightarrow 0$ as $\sigma_t \rightarrow \infty$.

Plugging into

$$\Sigma_t(\mathbf{x}_t) = \sigma_t^2 (\mathbf{I} + \sigma_t^2 \nabla^2 \log p(\mathbf{x}_t)) \quad (27)$$

gives

$$\Sigma_t(\mathbf{x}_t) = \sigma_t^2 \mathbf{I} + o(\sigma_t^2), \quad (28)$$

and hence $\lambda_k^t(\mathbf{x}_t) = \sigma_t^2 + o(\sigma_t^2)$ for all k . \square

This implies that at large noise, the posterior covariance becomes asymptotically isotropic; the spectrum *flattens* and “small” eigenvalues are lifted to $\approx \sigma_t^2$. Their contribution is therefore indistinguishable from isotropic noise, which explains why including late timesteps or many tail eigenvalues does not improve OOD discrimination.

A.5 Proof of Ky Fan’s Theorem

Prop. 2. Let $\Sigma_t(\mathbf{x}_t) \succeq 0$ have eigenvalues $\lambda_1^t \geq \dots \geq \lambda_n^t$ with eigenvectors forming $\mathbf{U}_t = [\mathbf{u}_1^t, \dots, \mathbf{u}_n^t]$. For any $K \in \{1, \dots, n\}$,

$$\max_{\mathbf{V} \in \mathbb{R}^{n \times K}: \mathbf{V}^\top \mathbf{V} = \mathbf{I}_K} \text{tr}(\mathbf{V}^\top \Sigma_t(\mathbf{x}_t) \mathbf{V}) = \sum_{k=1}^K \lambda_k,$$

and a maximizer is $\mathbf{V}^* = [\mathbf{u}_1^t, \dots, \mathbf{u}_K^t]$.

Proof. Let $\mathbf{V} \in \mathbb{R}^{n \times K}$ with $\mathbf{V}^\top \mathbf{V} = \mathbf{I}_K$. Write $\Sigma_t(\mathbf{x}_t) = \mathbf{U}_t \Lambda_t \mathbf{U}_t^\top$ with \mathbf{U}_t orthogonal. Set $\mathbf{Q} := \mathbf{U}_t^\top \mathbf{V} \in \mathbb{R}^{n \times K}$. Since \mathbf{U}_t is orthogonal, $\mathbf{Q}^\top \mathbf{Q} = \mathbf{V}^\top \mathbf{U}_t \mathbf{U}_t^\top \mathbf{V} = \mathbf{I}_K$, so the columns of \mathbf{Q} are orthonormal.

We have

$$\text{tr}(\mathbf{V}^\top \Sigma_t(\mathbf{x}_t) \mathbf{V}) = \text{tr}(\mathbf{V}^\top \mathbf{U}_t \Lambda_t \mathbf{U}_t^\top \mathbf{V}) = \text{tr}(\mathbf{Q}^\top \Lambda_t \mathbf{Q}) = \sum_{i=1}^n \lambda_i^t \|q_i\|_2^2,$$

where q_i^\top denotes the i -th row of \mathbf{Q} (so $\|q_i\|_2^2 \geq 0$). Because $\mathbf{Q}^\top \mathbf{Q} = \mathbf{I}_K$,

$$\sum_{i=1}^n \|q_i\|_2^2 = \text{tr}(\mathbf{Q}^\top \mathbf{Q}) = K, \quad \text{and} \quad \|q_i\|_2^2 \leq 1 \text{ for all } i \text{ (each row is a subvector of a unit vector).}$$

Thus the objective is a linear functional of the nonnegative weights $w_i := \|q_i\|_2^2$ subject to $\sum_i w_i = K$ and $0 \leq w_i \leq 1$. Since the eigenvalues are ordered $\lambda_1^t \geq \dots \geq \lambda_n^t$, the sum $\sum_i \lambda_i^t w_i$ is maximized by assigning $w_i = 1$ for $i = 1, \dots, K$ and $w_i = 0$ otherwise (rearrangement/greedy argument), which yields

$$\max_{\mathbf{V}^\top \mathbf{V} = \mathbf{I}_K} \text{tr}(\mathbf{V}^\top \Sigma_t \mathbf{V}) = \sum_{i=1}^K \lambda_i^t.$$

This maximum is attained by taking $\mathbf{Q} = [e_1, \dots, e_K]$, i.e., $\mathbf{V} = \mathbf{U}_t \mathbf{Q} = [\mathbf{u}_1^t, \dots, \mathbf{u}_K^t]$, the matrix of the top- K eigenvectors. \square

B Additional details

B.1 Computations of Eigenvalues

To compute the leading eigenvalues of the posterior covariance efficiently, we follow the Jacobian-free subspace iteration method introduced by [62]. The algorithm approximates Jacobian–vector products using finite differences of the denoiser output, followed by QR orthogonalization to stabilize directions. Iteratively refining these directions yields approximate posterior principal components and their corresponding eigenvalues. This approach avoids the costly explicit Jacobian calculation while still capturing the dominant spectral structure of the denoising uncertainty. Algorithm 2 reports the calculations of eigenvalues.

Algorithm 2 Efficient computation of posterior principal components [62]

Require: N (Number of PCs), K (number of iterations), $D(\cdot)$ (MSE-optimal denoiser), \mathbf{y} (noisy input), σ_t^2 (noise variance), $c \ll 1$ (linear approx. constant)

```
1: Initialize  $\{\mathbf{v}_0^{(i)}\}_{i=1}^N \sim \mathcal{N}(0, \sigma_t^2 \mathbf{I})$ 
2: for  $k \leftarrow 1$  to  $K$  do
3:   for  $i \leftarrow 1$  to  $N$  do
4:      $\mathbf{v}_k^{(i)} \leftarrow \frac{1}{2c} \left( D(\mathbf{y} + c\mathbf{v}_{k-1}^{(i)}) - D(\mathbf{y} - c\mathbf{v}_{k-1}^{(i)}) \right)$ 
5:   end for
6:    $\mathbf{Q}, \mathbf{R} \leftarrow \text{QR DECOMPOSITION} \left( [\mathbf{v}_k^{(1)} \cdots \mathbf{v}_k^{(N)}] \right)$ 
7:    $[\mathbf{v}_k^{(1)} \cdots \mathbf{v}_k^{(N)}] \leftarrow \mathbf{Q}$ 
8: end for
9:  $\mathbf{v}^{(i)} \leftarrow \mathbf{v}_K^{(i)}$ 
10:  $\lambda^{(i)} \leftarrow \frac{\sigma_t^2}{2c} \|D(\mathbf{y} + c\mathbf{v}_{K-1}^{(i)}) - D(\mathbf{y} - c\mathbf{v}_{K-1}^{(i)})\|$ 
```

Table 5: Optimized hyperparameters for EigenScore.

| InD OOD | CelebA vs. | | | C10 vs. | | | C100 vs. | | | SVHN vs. | | |
|-------------|-----------------------|-------------------|---------------|---------------|--------|--------|-----------|-----------|-----------|-----------------------------------|---|---------------------------------------|
| | C10 | C100 | SVHN | C100 | SVHN | CelebA | C10 | CelebA | SVHN | C10 | C100 | CelebA |
| Aggregation | All | All | All | Median | Median | All | All | Median | All | All | All | All |
| T | [100,150,200,250,300] | [100,150,200,250] | [150,200,250] | [100,150,200] | [150] | [100] | [100,150] | [450,500] | [150,200] | [100,150,200,250,300,350,400,450] | [100,150,200,250,300,350,400,450,500,550] | [100,150,200,250,300,350,400,450,500] |
| I | 20 | 20 | 20 | 20 | 20 | 20 | 20 | 20 | 20 | 20 | 20 | 20 |
| K | 3 | 3 | 3 | 3 | 3 | 3 | 3 | 3 | 3 | 3 | 3 | 3 |

B.2 Optimized parameters

We report the hyperparameters selected for EigenScore after validation. The aggregation method determines how repetitions are combined (mean, median, or none), while T specifies the set of diffusion timesteps, I the number of repetitions, and K the number of leading eigenvalues retained. These parameters were tuned on validation sets to balance accuracy and efficiency, and the final values are used consistently across experiments reported in the main paper in Table 1.

B.3 Baselines

We compare our method against several generative baselines for OOD detection, including Improved CD [70], DoS [46], TT [51], WAIC [5], NLL, IC, DDPM-OOD [3], LMD [36], DiffPath [35]. We use the official repositories for each method, along with diffusion models trained under the EDM framework [26] and the Glow model [45]. For the Glow-based baselines (DoS, TT, WAIC), we follow [46]. In DoS, we extract three statistics—the log-likelihood, latent log-probability, and Jacobian log-determinant—and fit Kernel Density Estimators (KDE) on the training data for each, summing across statistics to obtain the final score. For TT and WAIC, we adopt the sample-wise versions from [46]: TT measures the deviation of an individual sample’s likelihood from the training-set average, while WAIC is computed from five independently trained models using the mean and variance of their log-likelihoods. For diffusion-based baselines, we compute NLL using the official implementation from OpenAI’s improved diffusion Github repository¹ and derive IC by combining this NLL with PNG compression. Other methods (DDPM-OOD², LMD³, DiffPath⁴) are implemented using their official repositories.

B.4 Dataset and Models

We follow the official train/test splits when training diffusion models. For validation, we randomly sample 500 in-distribution (InD) and 500 OOD images; for testing, we sample a disjoint set of 500

¹<https://github.com/openai/improved-diffusion>²<https://github.com/marksgraham/ddpm-ood>³https://github.com/zhenzhel/lift_map_detect⁴<https://github.com/clear-nus/diffpath>

InD and 500 OOD images. All images are resized to 32×32 . All diffusion models are trained using the EDM framework of [26].